Linear drag law for high-Reynolds-number flow past an oscillating body

Natalie Agre,[1] Stephen Childress,[1] Jun Zhang,[1,2] and Leif Ristroph[1]

[1]*Applied Math Laboratory, Courant Institute, New York University, New York, New York 10012, USA*
[2]*Department of Physics, New York University, New York, New York 10003, USA*
and Department of Physics, New York University Shanghai, Pudong, Shanghai 200122, China

An object immersed in a fast flow typically experiences fluid forces that increase with the square of speed. Here we explore how this high-Reynolds-number force-speed relationship is affected by unsteady motions of a body. Experiments on disks that are driven to oscillate while progressing through air reveal two distinct regimes: a conventional quadratic relationship for slow oscillations and an anomalous scaling for fast flapping in which the time-averaged drag increases linearly with flow speed. In the linear regime, flow visualization shows that a pair of counterrotating vortices is shed with each oscillation and a model that views a train of such dipoles as a momentum jet reproduces the linearity. We also show that appropriate scaling variables collapse the experimental data from both regimes and for different oscillatory motions into a single drag-speed relationship. These results could provide insight into the aerodynamic resistance incurred by oscillating wings in flight and they suggest that vibrations can be an effective means to actively control the drag on an object.

A central goal of fluid dynamics is to relate the shape and motion of a body to the aerodynamic or hydrodynamic forces it experiences. Investigations into such force laws have formed the basis of fluid physics and engineering and have led to far-reaching applications [1], from minimizing drag by streamlining shapes to generating lift and thus enabling heavier-than-air flight [2]. Studies over the past two centuries have revealed fundamental scaling relationships relating forces to speed for the case of steady flow past a body or, equivalently, steady motion of a body through a fluid. For small objects in slow flows, forces vary in direct proportion to the speed, while large objects in fast flows experience forces that increase as the square of speed [1,3]. These linear and quadratic regimes are demarcated by the Reynolds number, which quantifies the relative importance of fluid inertia to viscosity. Large bodies in fast flows correspond to high Reynolds number and the well-known quadratic drag law stems from the separation of flow from the surface and the associated pressure difference across the body [4].

Strongly unsteady motions of a body in a flow are likely to significantly modify flow separation and thus alter force-speed scaling relationships. Such time-dependent motions are common in many contexts. For example, the flow-induced fluttering of flexible structures, such as the flapping of a flag, has recently been studied as an archetype of passively excited oscillations [5–7]. Animal locomotion provides examples in which oscillations of structures are actively driven, such as in flying or swimming propelled by flapping wings or fins [8–10]. One feature common to all these problems is the superposition of unsteady or ac motions and steady or dc motions. For the case of locomotion, for example, this involves the oscillations or flapping of an appendage superposed on the body translation during steady forward flight or swimming.

Here we aim to experimentally characterize how the addition of oscillations onto the otherwise steady motion of a structure affects the force-speed relationship. We seek an idealized situation of a simply shaped body undergoing a simple combination of sinusoidal and steady motions relative to a fluid. As illustrated in Fig. 1(a), we focus on the case of in-line oscillations of a thin disk within an oncoming steady flow, where the ac and dc motions are both normal to the plane of the disk. In terms of the passive and active contexts mentioned above, this situation is most analogous to in-line vibrations of a flexible structure in a flow or the back-and-forth flapping of an insect wing as it moves along with the body during forward flight. Rather than replicate these particular situations, we aim to
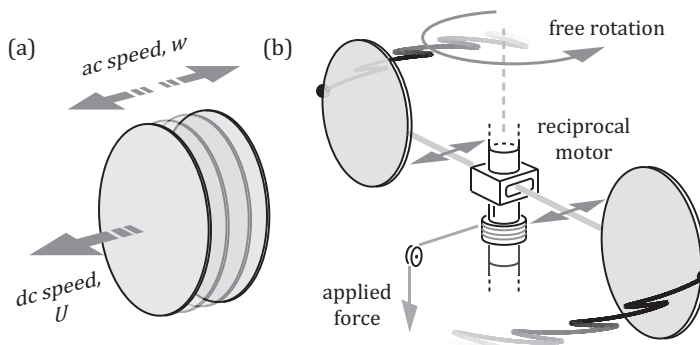
FIG. 1. (a) In-line oscillations of a translating disk in a flow. (b) Experimental apparatus: Disks are driven to oscillate back and forth by a motor and are free to rotate through air in response to an applied force.

abstract the problem in order to investigate the fluid mechanical consequences of combined dc and ac motions. Specifically, we will vary the relative magnitudes of the (time-averaged) ac speed w and the dc speed U in order to explore a range of fluid dynamic conditions, from purely steady to strongly unsteady. For dc-dominated conditions, one expects that local flows generated in one oscillation are left behind and do not strongly affect the next. The ac-dominated conditions, in contrast, could lead to strong body-vortex interactions that significantly alter the fluid forces.

I. EXPERIMENTS

A. Experimental setup and procedures

To characterize the effect of unsteady motions on drag, we devise an experimental apparatus that allows for direct force measurement on oscillating objects moving through air. As illustrated in Fig. 1(b), oscillations are driven by a reciprocating motor and the steady motion takes the form of rotation around a central vertical axis. More specifically, a pair of thin disks is connected via horizontal supports to a central housing, which itself is attached via low-friction rotary bearings to an upright axle. This allows for free rotation through air in response to an imposed external torque applied at the base. The disks attain a terminal rotation speed when the applied torque and aerodynamic resistance come into balance. Measurements of the terminal rotation speed for increasing applied torque can then be converted to yield a relationship between time-averaged drag and the translational speed at the center of each disk. This scheme thus involves imposing the force and measuring the resulting speed, which is an alternative to wind tunnel studies that impose the flow speed and measure the resulting force.

The drag incurred for steady or dc motions can be characterized by fixing the disks relative to the central housing, leading to simple revolving of the bodies about the vertical axle. To investigate the effect of ac motions, the on-board motor is powered and drives sinusoidal flapping of prescribed frequency and amplitude. The force-speed relationship is again obtained by sweeping through values for the applied force and measuring terminal rotation speed for specified oscillation kinematics. In this case, each disk undergoes unsteady motion through the air that is the superposition of ac and dc components, as illustrated by the trajectory of Fig. 1(b). For all cases, we employ a mass-string-pulley system to impose the external force: A mass falls under gravity and is fixed to a string that wraps around the central axle. The resulting terminal rotation speed is measured using a high-speed video camera that records the motion of the disks.

We report on measurements carried out for disks of diameter $d = 24$ cm whose centers are 27 cm from the axis of rotation. The disks are flapped at peak-to-peak amplitude $A = 3.5$ cm and frequency in the range $f = 5$–10 Hz. The average flapping speed $w = 2Af$ characterizes the ac
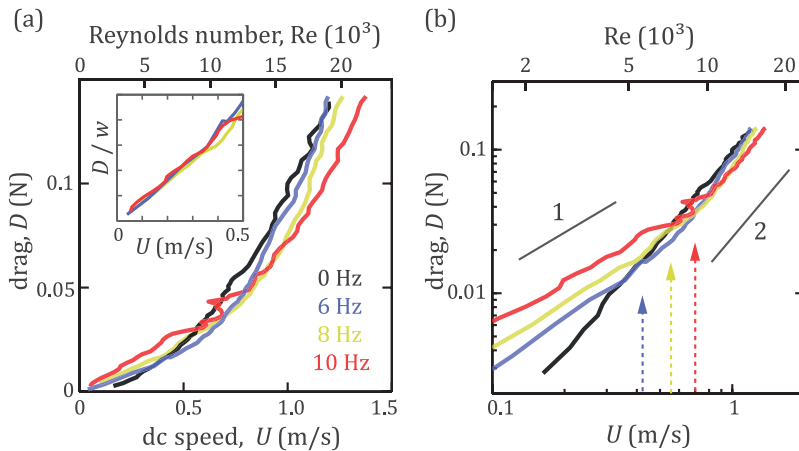
FIG. 2. Force-speed characterization. (a) Time-averaged drag D on each disk moving at steady dc speed U while driven to oscillate at frequencies $f = 6$, 8, and 10 Hz (blue, yellow, and red curves, respectively) and peak-to-peak amplitude $A = 3.5$ cm. The inset shows data collapse for D/w vs U. (b) Logarithm-scale plot of the same, revealing a linear drag-speed (slope 1) relationship for low U and conventional quadratic scaling (slope 2) for high U. Arrows indicate the state for which U equals the mean oscillation speed $w = 2Af$.

component of motion and the terminal speed U is the dc component. Typical parameter values lead to Reynolds numbers $\text{Re} = \rho U d/\mu \sim 10^3$–$10^4$, where ρ and μ are the density and viscosity of air, respectively [1,3]. The two relevant speeds U and w are of the same order and thus the Re defined using either is high ($\text{Re} \gg 1$), indicating the dominance of fluid inertial forces over viscosity. The relative magnitude of these two speeds, however, is expected to play a critical role in governing the drag. The ratio of dc to ac speeds $J = U/w$ is analogous to the advance ratio or inverse of the Strouhal number in other contexts of unsteady flow [8,10–12].

B. Measurement of drag for steady and unsteady motions

Considering first the case of purely steady motion, the black curve in Fig. 2(a) displays the dependence of drag D on speed U. The curve represents many individual measurements, each of which employs a mass-string-pulley system to impose the external force that balances drag at the terminal speed. The raw data are converted to yield a plot of the drag D on a single disk as its center moves at speed U. The apparent nonlinear increase of D with U can be quantified using a logarithm-scale plot, as shown in Fig. 2(b). The black curve shows that the data follow a line of slope 2 across all speeds, indicating a quadratic relationship $D \sim U^2$, as is expected for high-Reynolds-number flows [1,3]. Here the value of Re is labeled on the upper horizontal axes in Fig. 2, showing that $\text{Re} > 10^3$ for all experimental conditions. The black curve of Fig. 2(b) also shows that our measurement system captures the quadratic relationship down to forces as small as 3×10^{-3} N, which is several times greater than the force needed to overcome friction in our apparatus.

These data also allow us to infer the dimensionless drag coefficient for the case of steady motion, defined as $C_D^* = D/\frac{1}{2}\rho S U^2$, where $S = \pi d^2/4$ is the disk cross-sectional area. Applying a linear regression to the black data in Fig. 2(b), we measure a best-fit value of $C_D^* = 3.5 \pm 0.1$. We note that this coefficient is significantly greater than the value of 1.2 measured for a steadily translating disk at Reynolds numbers similar to those in our experiments [13]. The cause for this difference seems to be the form of the motion, that is, revolving versus translation. Nonetheless, our measurement quantitatively agrees with a value for the drag coefficient of 3.4 ± 0.1 obtained in

previous experiments for thin wings steadily revolved at a 90° angle of attack [14]. We interpret this close correspondence, even for somewhat different shapes, as a validation of our force measurement apparatus and procedure. This case of steady revolving motion, and the associated experimental value of C_D^*, will serve as a point of comparison for our force measurements for unsteady motions.

To investigate unsteady drag, we power the motor to drive oscillations of the disks at prescribed A and f and we again carry out the measurement procedure in which an external force is imposed and comes into balance with drag on the bodies at a terminal speed. In this work, we keep a peak-to-peak amplitude of $A = 3.5$ cm and employ six different frequencies in the range $f = 5$–10 Hz. The blue, yellow, and red curves of Fig. 2(a) represent the cases of flapping at selected frequencies of 6, 8, and 10 Hz, respectively. Just as for the steady case, each curve is composed of many points, each of which is collected by independent runs in which an external force is imposed and a terminal speed is measured. These data show that increasing frequency leads to stronger deviations from the steady drag-speed curve (black). This is most clearly seen in the logarithm-scale plot of Fig. 2(b). For example, for $f = 10$ Hz (red), the drag at low U is significantly higher than that of the steady case (black) and the slope of the $D(U)$ curve differs significantly from the conventional value of 2. In fact, the low-U data for each frequency is consistent with slope 1 or linear scaling, while at higher U each curve transitions to a quadratic scaling. The transition in scaling appears as a bend in each curve of Fig. 2(b) and seems to correspond to the condition in which the dc speed equals the time-averaged ac speed $U \approx w$, as indicated by the arrows.

These measurements also allow us to examine the dependence of drag on the flapping speed $w = 2Af$ for sufficiently small U. As can be seen in Fig. 2(b), the upward shift in the curves for increasing f suggests that drag increases with w. Indeed, as shown by the inset of Fig. 1(a), plotting D/w vs U collapses all data sets with $f > 0$, implying that D scales linearly with w when U is small.

Taken together, these experiments for unsteady motions reveal two distinct drag scaling regimes demarcated by the speed ratio $J = U/w$. The quasisteady or dc-dominated regime for $J > 1$ is characterized by the conventional quadratic drag-speed law $D \sim U^2$. The unsteady or ac-dominated regime for $J < 1$ is characterized by drag scaling as the product of the dc and ac speeds $D \sim Uw$.

C. Dimensionless drag-speed relationship

To unify these observations across different unsteady motions, we consider dimensionless forms for the time-averaged speed of motion and the time-averaged fluid force experienced. The speed ratio $J = U/w$ is a natural choice, with $J < 1$ signifying unsteady or ac-dominated motions and $J > 1$ signifying steady or dc-dominated motions. As a normalization of force, we choose the drag coefficient $C_D = D/\frac{1}{2}\rho S U^2$, defined exactly as is done for steady motion at speed U for a body of area S in a fluid of density ρ. We note that other dimensionless forms of the force could be employed, in particular coefficients based on other choices for the speed scale such as w, $\sqrt{Uw}$, $\sqrt{U^2 + w^2}$, etc. Our choice to use U, which is the average speed relative to the far-field fluid, allows one to directly compare the drag experienced for an unsteady motion at a given J to steady motion at the same average speed. This involves comparing $C_D(J)$ to C_D^*, the steady drag coefficient. Further, as we show below, our selections of these dimensionless quantities leads to a unification of the force-speed data in terms of $C_D(J)$ curves.

In Fig. 3(a) we plot C_D versus J and arrive at a collapse of the experimental data across all six measured frequencies ($f = 5$–10 Hz) and for both scaling regimes. As a point of comparison, we show the experimentally measured steady drag coefficient value $C_D^* = 3.5$ as a dashed horizontal line. To interpret this plot, one can consider the effect of adding oscillations to a disk undergoing motion at speed U. Without oscillations, the force coefficient is C_D^* and one can see that adding unsteady motion can either increase or decrease the force coefficient C_D depending on J. For exceedingly slow oscillation speeds of $J \gg 1$, the drag is similar to the steady case $C_D \approx C_D^*$, as is expected. For exceedingly fast oscillations of $J \ll 1$, the time-averaged drag is significantly larger
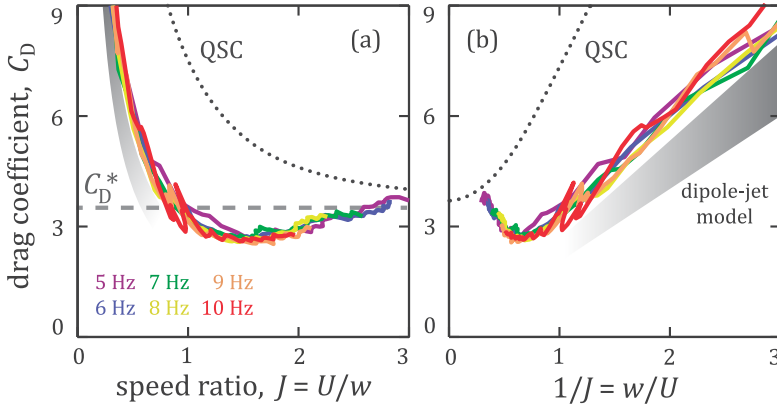
FIG. 3. Normalization reveals a universal drag-speed relationship for unsteady motions. (a) Drag coefficient $C_D = D/\frac{1}{2}\rho S U^2$, where S is the disk area, plotted vs the speed ratio $J = U/w$. The dashed line indicates the experimentally measured value of $C_D^* = 3.5 \pm 0.1$ for steady motion and colored curves represent six cases of unsteady motions with different values of f. (b) Plotting C_D vs $1/J$ emphasizes the unsteady regime $1/J > 1$. Also shown are predictions of a quasisteady calculation (dotted curves) and an unsteady dipole-jet model (gray bands). See the text for model details.

than that for steady motion. In addition, one can see that a drag reduction occurs for moderate oscillations of $1 < J < 2$.

The strong drag amplification occurs in the unsteady regime of $J < 1$. To emphasize these ac-dominated conditions, we display C_D vs $1/J$ in Fig. 3(b), where now increasing unsteadiness occurs to the right in the plot. This form shows that C_D scales linearly with $1/J$ for large $1/J$, which is simply a dimensionless form for the unsteady drag law inferred earlier: $C_D \sim 1/J$ is equivalent to $D/U^2 \sim w/U$ and thus $D \sim Uw$. Having established this relationship in the unsteady regime, our central goals are to understand the flows involved under these conditions and to use these findings to formulate a mathematical model capable of reproducing this unsteady drag law.

D. Flow visualization

To understand the fluid dynamic origin of these scaling regimes, we visualize the flows produced by a flapping disk [15]. Here we use a visualization water tunnel that provides a laminar flow and whose test section is custom fitted with a motor assembly that drives oscillations. Maintaining a similar Re as in the previous experiments, we explore the effect of varying $J = U/w$, where U is the speed provided by the tunnel and w is set by the motor assembly. In one method, fluorescein dye is released from the front of the disk near the stagnation point, spreads over the front surface, and washes off the disk edge. The resulting streaklines shown in Figs. 4(a)–4(c) highlight the vorticity generated by the edge motion [1]. In a second technique, we seed the water with glass microparticles, illuminate a plane with a laser sheet, and capture time-exposed photographs, as shown in Fig. 4(d). The resulting particle pathlines give an indication of the flow velocity field over a plane. This technique is particularly well suited for fast flapping conditions, in which case dyes tend to rapidly disperse and homogenize.

The steady case ($w = 0$) is shown in Fig. 4(a) as well as [16], where the flow past a stationary disk separates off the edge and forms an unstable wake downstream. In contrast, Fig. 4(b) shows that even relatively gentle flapping of $J \approx 2$ leads to a qualitatively different separated flow region. Captured here during the forward stroke, the disk motion leads to a large and coherent vortex ring that curls up around the edge. The back-and-forth motion generates the pair of counterrotating vortex rings that can be seen downstream. Shedding of such vortex pairs, or dipoles [17], has also been observed in other cases of oscillatory flows past an object [18–21]. The close-up photograph of
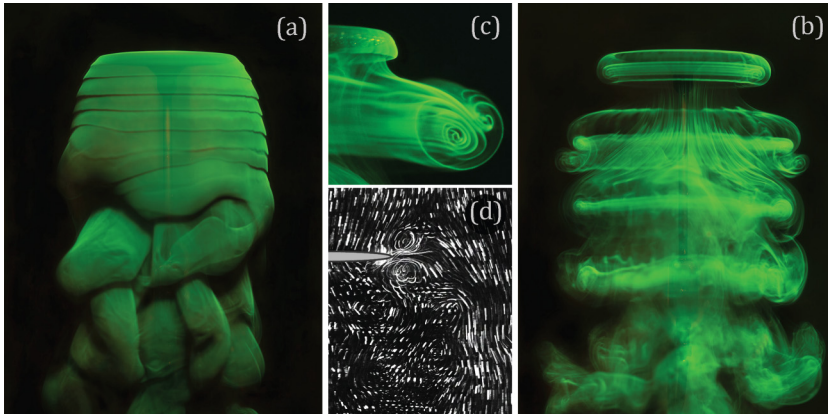
FIG. 4. Visualization of flow past stationary and oscillating disks (see movies in the Supplemental Material [16]). (a) Fluorescein dye streaklines reveal the flow (top to bottom) past a stationary disk oriented horizontally near the top of the photograph. (b) Streaklines for a flapping disk with speed ratio $J = U/w \approx 2$. (c) Close-up of an asymmetric dipole generated under the same conditions. (d) Time-exposed photograph of glass microspheres illuminated by a laser sheet reveal flow path lines for faster flapping ($J \approx 0.5$). A more symmetric dipole is generated near the disk edge and these dipoles lose their coherence further downstream.

Fig. 4(c) captures a highly asymmetric dipolar ring, whose constituent vortices differ strongly in size and intensity. Faster flapping of $J \approx 0.5$ produces more symmetric dipoles, as shown in Fig. 4(d). In this case, the dipoles quickly lose their coherence as they propagate outward from the disk edge.

These visualization studies identify vortex dipoles as prominent local flow structures in the unsteady regime of fast oscillations. At a given dc speed U, fast oscillations ($J \ll 1$) tend to form intense and relatively symmetric dipoles, while slower oscillations ($J \lesssim 1$) tend to form weaker and more asymmetric dipoles. In what follows, we will consider a mathematical model that calculates the strength and asymmetry of such dipoles from the motion of the body and then uses the dynamics of these vortex pairs to estimate the drag on the body.

II. MATHEMATICAL MODEL

A. Quasisteady calculation

As a first step towards a mathematical model, we consider a quasisteady calculation of the aerodynamic drag, as is often used to estimate the forces on wings undergoing flapping motions [22–31]. Such calculations approximate the instantaneous force during an unsteady motion by that experienced for steady motion under the same conditions, i.e., at the same speed and angle of attack. For the problem considered here, a disk moves at an attack angle of $90°$ and instantaneous velocity $u(t) = U + \frac{\pi}{2} w \sin(2\pi f t)$. Within the quasisteady calculation (QSC), the instantaneous drag is $-\frac{1}{2}\rho S C_D^* u|u|$, D is its time average over an oscillation cycle, and $C_D = D/\frac{1}{2}\rho S U^2$ is the nondimensional form. Using MATLAB to numerically compute the integral associated with time averaging, we arrive at the solution displayed as the dotted curve $C_D(J)$ labeled QSC in Fig. 3(a).

Because the QSC is based on approximating the instantaneous force by that experienced under steady conditions, one expects it to be most accurate when the ac speed w is a small perturbation to the dc speed U, that is, for $J = U/w \gg 1$. Indeed, Fig. 3(a) shows that the QSC curve and the experimental data both approach the steady drag coefficient C_D^* for large J. Further, we note that in this quasisteady regime of $U \gg w$, the velocity resulting from the combined dc and ac motions is strictly positive, in which case the integral for time-averaged drag can be solved analytically, yielding $C_D = C_D^*(1 + \pi^2/8J^2)$. Thus, the QSC predicts an approach of C_D to C_D^* from above as J increases, while the experimental curves of Fig. 3(a) show an approach from below. Overall, the
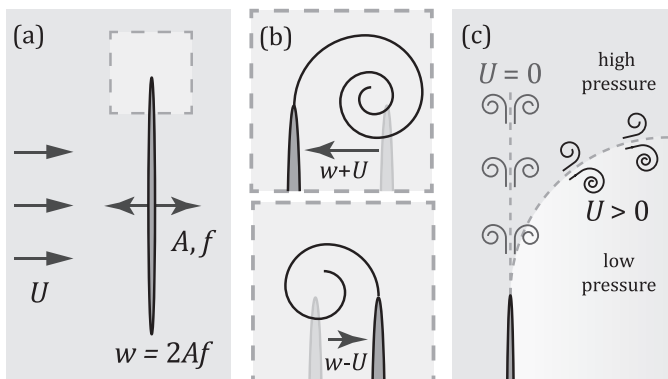
FIG. 5. A train of vortex dipoles can be modeled as a jet. (a) A plate flaps with frequency f, peak-to-peak amplitude A, and average speed $w = 2Af$ in an oncoming flow of speed U. (b) The forward stroke generates a clockwise vortex and the backward stroke produces a counterrotating vortex. Together, a complete stroke creates a vortex pair. (c) Repeated oscillations create a train of dipoles that can be viewed as a jet. The jet is emitted straight outward for $U = 0$ and curves downstream for $U > 0$.

QSC seems accurate only in predicting the limiting value $C_D(J \to \infty) = C_D^*$, but does not account for the asymptotic scaling.

One expects the QSC to fare even worse for highly unsteady motions. Indeed, for $J < 1$, the QSC tends to overpredict the forces by more than a factor of 2, as is apparent in Fig. 3(a) and more clearly in the plot of $C_D(1/J)$ in Fig. 3(b), which accentuates the unsteady regime.

While not quantitatively accurate for the unsteady limit of interest in this work, the QSC does recover the scaling relationship $C_D \sim 1/J$ observed in experiments for $J < 1$. This scaling is most clearly seen in the dotted curve of Fig. 3(b), which approaches a line for large $1/J$. Within the quasisteady framework, this scaling can be motivated by a simple calculation: The forward stroke of the disk has a speed $u \sim w + U$ and a negative force (resisting U), while the backward stroke has a slower speed $u \sim w - U$ and a positive force. The magnitude of the time-averaged force over a complete cycle thus scales as $D \sim -(w + U)^2 + (w - U)^2 \sim Uw$. As discussed earlier, $D \sim Uw$ is equivalent to the dimensionless form $C_D \sim 1/J$. It is somewhat surprising that the QSC recovers the observed force-speed scaling in the unsteady regime, even though the quasisteady assumption of $U \gg w$ or $J \gg 1$ is strongly violated.

The QSC is thus successful in recovering the scaling and order of magnitude of the forces but is not quantitatively accurate in the unsteady regime and, because it has no sound physical basis under these conditions, it is difficult to conceive of improvements within the quasisteady framework. This motivates the formulation of a mathematical model that is explicitly rooted in the unsteady flows generated by an oscillating body. Below we consider an intrinsically unsteady model with the goals of furnishing more accurate force estimates in the fast flapping or low-J limit as well as providing a physical explanation for the $C_D \sim 1/J$ scaling relationship.

B. Dipole-jet model: Overview and key results

Here we provide a brief overview of the mathematical model, including the key findings, and in the sections that follow we outline the steps and calculations in detail. Inspired by the visualization experiments, we seek a model that relates drag to the formation and dynamics of vortices and focus in particular on the limit of fast flapping motions. In this case $J \ll 1$ and the oncoming dc speed U can be viewed as a small perturbation to the condition of pure oscillations of average speed w. We consider the two-dimensional (2D) situation of an oscillating plate in a flow and we assume that a dipole is created at each edge during a back-and-forth cycle, as shown in Figs. 5(a) and 5(b). The

unperturbed state ($U = 0$) generates a symmetric dipole in which each constituent vortex has equal strength. A single dipole in a fluid tends to propagate [17] and we assume that repeated oscillations form an array of dipoles that propagate outward, as sketched in Fig. 5(c). In our model, we associate this train of discrete dipoles with a continuous jet [1,3] or localized region of fast flow extending outward from the disk edge.

As illustrated in Fig. 5(b), the perturbed state ($U > 0$) involves a faster relative speed on the forward stroke than on the backward stroke, generating an asymmetric dipole with each complete oscillation. In isolation, such a structure propagates but also rotates due to the unbalanced vorticity, leading to a curved trajectory [3,17]. In our model, this effect is associated with a curved centerline of the jet, as shown in Fig. 5(c). Importantly, our model takes advantage of the fact that the curvature of a jet serves as a signature of the pressure difference that induces its bending [32]. By calculating this jet pressure differential and assuming it to also act across the body itself, our model ultimately relates drag to the dc and ac speeds.

To make a quantitative comparison of the dipole-jet model (DJM) to the experimental data, the calculations below consider a spectrum of spatial distributions of vorticity within the emitted jet. This ranges from two vortex sheets bounding an irrotational core to two adjacent regions of uniform vorticity. For all such jet geometries, we recover the scaling $C_D \sim 1/J$ and the multiplicative coefficient relating these two quantities is found to vary relatively little, from 2 to 2.7. These different solutions are shown together as the gray band labeled as the dipole-jet model in Fig. 3(b), where the gradient in the band emphasizes that the model applies in the large-$1/J$ limit. The DJM can be seen to somewhat underpredict the measured drag. To quantify this, we use a linear regression to measure the coefficient relating C_D and $1/J$ in the experimental data, finding $C_D \approx (3.0 \pm 0.2) \times 1/J$. Thus, while the QSC overestimates the measurements with relative error of about 100%, the DJM underestimates the drag with smaller error of about 20%. Importantly, as discussed below, the DJM also offers a clear fluid dynamical mechanism behind the unsteady drag-speed relationship and suggests possible improvements in these force estimates.

C. Determining vorticity from flapping motions

The work of Schnipper *et al.* [33] furnishes an estimate for the total or area-integrated vorticity ejected at separation off a sharp edge in unsteady motion. Their calculation relies on the integration of vorticity across a boundary layer of flow profile $u_{BL}(y)$ and thickness δ as it is being ejected to form a vortex or eddy of circulation Γ. Here $u_{BL}(0) = 0$ on the body surface and $u_{BL}(\delta)$ represents the flow speed just outside the boundary layer. Then the circulation is given by

$$\Gamma = \iint_{\text{eddy}} \vec{\omega} \cdot d\vec{S} = \iint_{\text{edge}} u_{BL} \frac{du_{BL}}{dy} dy \, dt = \int \frac{1}{2} u_{BL}^2(\delta) dt.$$

One might assume that $u_{BL}(\delta)$ is given by the instantaneous speed of the plate edge relative to the fluid at infinity. Schnipper *et al.* suggest that such a calculation somewhat underestimates the vorticity generated. Here we assume

$$\Gamma = k \int \frac{1}{2} u^2(t) dt, \tag{1}$$

where k is a dimensionless prefactor and $u(t)$ is the instantaneous speed of the plate. In what follows, we retain k throughout all calculations but ultimately choose $k = 1$, which Schnipper *et al.* argue applies to boundary layer separation for steady flow over a body.

For the flapping motions studied here, the velocity at the plate edge is given by $\pi f A \sin(2\pi f t)$. During each half stroke, the above calculation yields a circulation of magnitude

$$\Gamma_0 = k \frac{1}{2} (\pi f A)^2 \int_0^{1/2f} \sin^2(2\pi f t) dt = \frac{k \pi^2 A^2 f}{8}. \tag{2}$$

The forward stroke generates the vorticity $-\Gamma_0$ on the right side of the dipole, as dictated by the right-handed convention. Likewise, the backward stroke generates the left side of vorticity $+\Gamma_0$. This provides an estimate for the total vorticity, however its distribution in space has yet to be specified.

If there is a (small) dc speed U, the relative speed at the plate edge is now $u = \pi f A \sin(2\pi f t) + U$ for the forward and backward strokes, respectively. The motion then generates an asymmetric dipole of unbalanced vorticity and it can be shown from Eq. (1) that the forward stroke produces a total vorticity of

$$\Gamma_1 = -\Gamma_0 - \Delta\Gamma, \tag{3}$$

where

$$\Delta\Gamma \approx kUA. \tag{4}$$

Here we have retained up to first-order terms in the small parameter U/w. Similarly, on the backstroke the total vorticity generated is

$$\Gamma_2 = \Gamma_0 - \Delta\Gamma. \tag{5}$$

In what follows, we distribute these eddies into a continuous jet and determine from the jet momentum and curvature the pressure decrement aft of the body. This will furnish an estimate of drag since the weak translational speed U contributes negligibly to the pressure difference.

D. Train of vortex dipoles as a jet

An isolated symmetric dipole tends to propagate along a straight trajectory and for point vortices with spacing $2a$ it is well known that the dipole will move with speed

$$U_d = \frac{\Gamma_0}{4\pi a} = \frac{k\pi A^2 f}{32a}. \tag{6}$$

See, for example, the texts by Batchelor [3] or Saffman [17]. Asymmetric dipoles propagate but also turn toward the stronger member of the pair. Repeated oscillations of the plate emit a dipole array or train that propagates straight outward for the case of $U = 0$ and curves downstream for $U > 0$, as shown in Fig. 5(c).

It is not immediately clear, however, how to compute the drag on the plate directly from the dipole dynamics. The key step in our model is to associate a train of discrete dipoles with a continuous jet, that is, a thin region of high-speed flow. Qualitatively, the dipole speed U_d sets the scale of the jet speed and the dipole spacing $2a$ sets the jet width. A straight jet is produced for $U = 0$ and a curving jet for $U > 0$. In what follows, we build up the vorticity and velocity distributions in the jet from the dipoles generated.

For $U = 0$, we spread the vorticity in each half of the symmetric dipole train into continuous bands on the outside of the jet, as shown in Fig. 6(a). Positive vorticity ω is distributed on the left side and negative vorticity of equal strength on the right. These regions bound an irrotational core of $\omega = 0$. Integrating ω across the jet gives its velocity profile u and plots of these quantities are shown in Fig. 6(b). Here we assume the width of the jet to be $2a$ and the parameter α defines the width of the irrotational core.

For $U > 0$, the train of asymmetric dipoles corresponds to a curving jet of asymmetric vorticity distribution and a corresponding velocity profile, as shown in Figs. 6(c) and 6(d). In all cases, with the velocity distribution specified, one can compute the pressure difference across the jet under the assumption of inviscid flow using the Euler equations. For $U = 0$, the pressure difference is zero, as is expected by symmetry, and one also expects zero drag across the plate. For $U > 0$, the flow field in cylindrical coordinates has zero radial component $u_r = 0$ and nonzero angular component u_θ, therefore the pressure difference across the curved or perturbed jet is given by $\Delta p = \rho \int_{\mathrm{PJ}} \frac{u_\theta^2}{r} dr$.
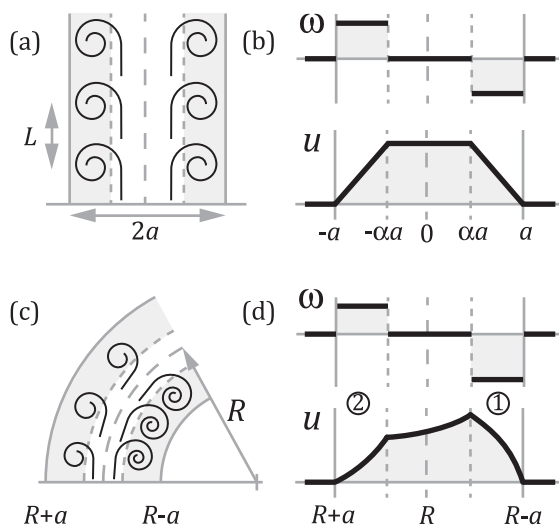
FIG. 6. A train of vortex dipoles can be viewed as a continuous jet. (a) The vorticity associated with symmetric dipoles can be spread into outer regions (gray regions) that bound an irrotational core. (b) Vorticity ω and velocity u profiles across the jet. Asymmetric dipoles tend to propagate and turn. A train of such dipoles can be viewed as a curving jet. (c) The inside of the jet (region 1) is of more intense vorticity than the outside (region 2) and the jet has radius of curvature R. (d) Vorticity ω and velocity u profiles across the jet.

It can be shown that keeping only first order in U/w yields

$$\Delta p \approx \rho \frac{1}{R} \int_{\mathrm{UJ}} u^2 dx, \tag{7}$$

where R is the radius of curvature of the perturbed jet and the integral is over the straight or unperturbed jet.

E. Unperturbed jet

In the unperturbed jet, the assumption of uniform vorticity exterior regions bounding an irrotational core leads to a velocity field [Fig. 6(b)] of the form

$$u = \begin{cases} \omega_0(x + a), & -a \leqslant x < -\alpha a \\ \omega_0 a(1 - \alpha), & -\alpha a \leqslant x \leqslant \alpha a \\ \omega_0(a - x), & \alpha a < x \leqslant a. \end{cases}$$

Here ω_0 is the strength of vorticity generated in each half stroke, a is the half width of the jet, and α defines the width of the irrotational core. We will retain these jet geometry parameters a and α in the calculations that follow and later explore the sensitivity of our results to variations in these quantities. As required for Eq. (7), we then compute

$$\int_{UJ} u^2 dx = \frac{2}{3} \omega_0^2 a^3 (1 - \alpha)^2 (1 + 2\alpha). \tag{8}$$

Next we determine ω_0 through Eqs. (1) and (2). We uniformly spread the vorticity produced in each vortex over a rectangular region on each side of the jet. The circulation of Eq. (1) is simply

$$\Gamma_0 = \iint \vec{\omega}_0 \cdot d\vec{S} = \omega_0 a(1 - \alpha)L,$$

where $a(1 - \alpha)$ is the width of each exterior vorticity band and

$$L = U_d/f = \frac{k\pi A^2}{32a} \tag{9}$$

is the distance between successive dipoles or, equivalently, the distance a dipole travels in one flap of the plate. Equivalently,

$$\omega_0 = \frac{\Gamma_0}{a(1 - \alpha)L}. \tag{10}$$

F. Perturbed jet

Now switching to cylindrical coordinates for the curving jet, we solve for the velocity field by integrating $\vec{\omega} = \vec{\nabla} \times \vec{u} = \frac{1}{r}\frac{\partial}{\partial r}(ru_\theta)\hat{z}$. Here r is the radial distance from the center of the jet and the simplified form of the curl results from only the angular component of the velocity u_θ being nonzero. In the outer regions, uniform vorticity implies that $u_\theta \sim r + \frac{1}{r}$. The center region of irrotational flow has the form $u_\theta \sim \frac{1}{r}$. Imposing the boundary condition that $u_\theta = 0$ on the outer boundaries and continuity conditions between the three regions gives the full velocity profile as well as the radius of curvature R of the jet. Here we are restricting our attention to a small segment of the jet emerging from the tip so that the radius of curvature may assumed to be constant:

$$u_\theta = \begin{cases} \frac{1}{2}\omega_1\left[r - \frac{(R-a)^2}{r}\right], & R - a \leqslant r < R - \alpha a \\ a^2(\alpha^2 - 1)\frac{\omega_1\omega_2}{\omega_1 + \omega_2}\frac{1}{r}, & R - \alpha a \leqslant r \leqslant R + \alpha a \\ \frac{1}{2}\omega_2\left[r - \frac{(R+a)^2}{r}\right], & R + \alpha a < r \leqslant R + a. \end{cases} \tag{11}$$

Here it can be shown that $R = \frac{a}{2}(\alpha + 1)\frac{\omega_1 - \omega_2}{\omega_1 + \omega_2}$.

As in Eq. (10), we integrate the uniform vorticity in the outer bands of the jet to arrive at $\omega_{1,2} = \frac{\Gamma_{1,2}}{a(1 - \alpha)L}$. This allows us to express the radius of curvature in terms of the total vorticity of the symmetric jet Γ_0 and its perturbation $\Delta\Gamma$,

$$R = \frac{a}{2}(\alpha + 1)\frac{\Gamma_0}{\Delta\Gamma}. \tag{12}$$

G. Pressure differential and drag

Using the results of Eqs. (8), (10), and (12), Eq. (7) then becomes

$$\Delta p = \frac{4}{3}\rho\frac{\Gamma_0\Delta\Gamma}{L^2}\frac{1 + 2\alpha}{1 + \alpha}.$$

Using Eqs. (2), (4), and (9) we can now relate the pressure difference to the kinematic variables U, A, and f. This leads to a drag coefficient of

$$C_D = \frac{\Delta p}{\frac{1}{2}\rho U^2} = \frac{512}{3}\frac{1 + 2\alpha}{1 + \alpha}\left(\frac{a}{A}\right)^2\frac{w}{U}, \tag{13}$$

where $w = 2Af$ is the average flapping speed.

The jet width $2a$ is yet to be determined in terms of the flapping motion of the plate. One prescription demands that the average jet speed u_J is equal to the dipole propulsion speed U_d, a choice that achieves consistency between the dipole and jet pictures. For the average jet speed we again make use of the velocity profile in the unperturbed jet:

$$u_J = \frac{1}{2a}\int_{UJ} u\, dx = \frac{\omega_0 a}{2}(1 - \alpha^2).$$

Taken together with Eq. (2), (10), and (9), we arrive at

$$u_J = 2\pi af(1 + \alpha). \tag{14}$$

Equating this to the dipole speed in Eq. (6), we arrive at the ratio $(\frac{a}{A})^2 = \frac{k}{64}\frac{1}{(1+\alpha)}$. Invoking the assumption of $k = 1$ from Eq. (1) gives $(\frac{a}{A})^2 = \frac{1}{64}\frac{1}{(1+\alpha)}$. The drag coefficient then becomes

$$C_D = \frac{8k}{3}\frac{1+2\alpha}{(1+\alpha)^2}\frac{w}{U} = \frac{8}{3}\frac{1+2\alpha}{(1+\alpha)^2}\frac{w}{U}. \tag{15}$$

This central result of the DJM shows that $C_D \sim w/U = 1/J$, which is the scaling measured in experiments in the unsteady limit of large $1/J$.

Finally, we explore how C_D is affected as α is varied over its entire range $0 \leqslant \alpha \leqslant 1$. Plotting $C_D(1/J)$ for all values of α leads to the gray band shown in Fig. 3(b). When $\alpha = 1$, the jet is a region of irrotational flow bounded by two vortex sheets and $C_D = 2 \times 1/J$. At the other extreme $\alpha = 0$, we have a jet composed of two regions of uniformly distributed vorticity and $C_D = \frac{8}{3} \times 1/J$. Thus, the predicted drag is relatively insensitive to the details of the vorticity distribution within the jet. Further, because of the assumption $k = 1$, we expect this model to somewhat underestimate C_D and indeed Fig. 3(b) shows that the DJM underestimates the experimental data by about 20%.

III. DISCUSSION

In this work we explore how the drag or aerodynamic resistance of a body in a flow is affected by unsteady motions and our idealized experiments involve a disk that is driven to oscillate while progressing through air. Our force measurements for different oscillation (ac) and steady (dc) speeds reveal two regimes: Slow oscillations lead to a drag that increases with the square of the dc speed and fast oscillations lead to a time-averaged drag that increases linearly with flow speed. This latter unsteady regime is the focus of this work, and experiments and modeling reveal the scaling law $D \sim Uw$, where U and w are the dc and ac speeds, respectively. This relationship lends itself to two physical interpretations for bodies undergoing fast oscillations in a flow. For fixed speed U of the body relative to the far-field fluid, the drag can be modulated in proportion to the flapping speed w. Similarly, for a body subject to a fixed force, its terminal speed U through the fluid can be slowed by increasing w.

The key physical insight provided by our dipole-jet model lies in the fact that faster oncoming flow speed U leads to more asymmetric dipoles and a more strongly curved jet. This produces a narrower wake downstream, as suggested by the schematic of Fig. 5(c). Counterintuitively, increasing U thus leads to an apparent streamlining, or diminished disturbance to the oncoming current by the body. In essence, the effective area S of the body presented to the flow decreases with increasing U and thus drag grows more weakly than the conventional U^2 scaling. For example, if the effective area decreases as $S \sim 1/U$, then $D \sim SU^2 \sim U$, which is the scaling relationship measured in experiments and recovered by our model.

While the quasisteady framework applies in the dc-dominated limit ($J \gg 1$) and our dipole-jet model applies in the ac-dominated limit ($J \ll 1$), the experimental data in the transitional region between these regimes show a number of features yet to be explained. We first note that $J = 1$ represents an unusual dynamical condition: The disk is nearly still relative to the fluid on the backward stroke when the ac and dc motions largely cancel and it then advances quickly on the forward stroke when the motions add. Interestingly, $J \approx 1$ seems to demarcate a surprisingly sharp transition between scaling regimes, as revealed by the kinks in the curves of Fig. 2(b). Other oddities include large variations in forces at $J \approx 1$ for higher f, as well as a pronounced drop in C_D near $J = 1.5$ [Fig. 3(a)]. This drop in C_D in particular, together with the high C_D for $J < 1$, indicates that drag can be either decreased or increased by the superposition of an ac oscillation on a steady dc motion. This suggests that imposed vibrations may be an effective means to modulate the resistance of a body to motion through a fluid [34].

Additional topics and parameters to be explored include system dimensionality (2D plate vs 3D disk), translational versus rotational motions, body shape, and kinematic parameters such as amplitude. To quantitatively assess the dipole-jet model predictions of the flows generated, future studies will involve two-dimensional experiments using a long plate undergoing fast flapping. Computational fluid dynamics simulations will also likely prove advantageous in comparing both the flows and forces to the predictions of this model [18,34]. Finally, unsteady fluid forces might also be inferred from quantitative measurements of the flow velocity field [35].

Animal flight provides analogs to the two regimes studied here, where $J > 1$ is represented by gliding and fast forward flight and $J < 1$ by hovering and slow maneuvering. Because natural flight involves wing shapes and flapping kinematics that differ markedly from those studied here, it is unclear whether the anomalous scaling for $J < 1$ is manifest among natural hoverers or flapping-wing robots. Interestingly, numerous recent studies have shown flight dynamics that are in fact consistent with a linear resistance to motion [22–31]. For example, measurements of the turning dynamics of animals [22,23,25,27,28,36,37] indicate a countertorque that is proportional to the body rotation speed. Similarly, the forward flight of insects [24] and robots [29] are also consistent with a linear drag-speed relationship. These observations suggest that the basic physical mechanisms studied in our idealized system may also be at work for more complex shapes and motions.

ACKNOWLEDGMENT

---

[1] D. J. Tritton, *Physical Fluid Dynamics* (Clarendon, Oxford, 1988).

[2] J. D. Anderson, *A History of Aerodynamics* (Cambridge University Press, Cambridge, 1997).

[3] G. K. Batchelor, *An Introduction to Fluid Dynamics* (Cambridge University Press, Cambridge, 2000).

[4] H. Schlichting and K. Gersten, *Boundary Layer Theory* (Springer, Berlin, 2000).

[5] J. Zhang, S. Childress, A. Libchaber, and M. Shelley, Flexible filaments in a flowing soap film as a model for one-dimensional flags in a two-dimensional wind, Nature (London) **408**, 835 (2000).

[6] M. Argentina and L. Mahadevan, Fluid-flow-induced flutter of a flag, Proc. Natl. Acad. Sci. USA **102**, 1829 (2005).

[7] M. Shelley, N. Vandenberghe, and J. Zhang, Heavy Flags Undergo Spontaneous Oscillations in Flowing Water, Phys. Rev. Lett. **94**, 094302 (2005).

[8] R. M. Alexander, *Principles of Animal Locomotion* (Princeton University Press, Princeton, 2003).

[9] S. P. Sane, The aerodynamics of insect flight, J. Exp. Biol. **206**, 4191 (2003).

[10] Z. J. Wang, Dissecting insect flight, Annu. Rev. Fluid Mech. **37**, 183 (2005).

[11] N. Vandenberghe, J. Zhang, and S. Childress, Symmetry breaking leads to forward flapping flight, J. Fluid Mech. **506**, 147 (2004).

[12] S. Alben and M. Shelley, Coherent locomotion as an attracting state for a free flapping body, Proc. Natl. Acad. Sci. USA **102**, 11163 (2005).

[13] F. W. Roos and W. W. Willmarth, Some experimental results on sphere and disk drag, AIAA J. **9**, 285 (1971).

[14] M. H. Dickinson, F.-O. Lehmann, and S. P. Sane, Wing rotation and the aerodynamic basis of insect flight, Science **284**, 1954 (1999).

[15] N. Agre, S. Childress, J. Zhang, and L. Ristroph, Comparative flow visualization for steady and unsteady motions of a disk through a fluid, Phys. Fluids **27**, 091103 (2015).

[16] See Supplemental Material at http://link.aps.org/supplemental/10.1103/PhysRevFluids.1.033202 for flow visualization movies.

[17] P. G. Saffman, *Vortex Dynamics* (Cambridge University Press, Cambridge, 1992).

[18] H. A. Khaledi, H. I. Andersson, M. Barri, and B. Pettersen, Flow past a normal flat plate undergoing inline oscillations, Phys. Fluids **24**, 093603 (2012).

[19] M. Canals and G. Pawlak, Three-dimensional vortex dynamics in oscillatory flow separation, J. Fluid Mech. **674**, 408 (2011).

[20] J. J. Williams, N. Metje, L. E. Coates, and P. R. Atkins, Sand suspension by vortex pairing, Geophys. Res. Lett. **34**, 15 (2007).

[21] O. M. Griffin and S. E. Ramberg, Vortex shedding from a cylinder vibrating in line with an incident uniform flow, J. Fluid Mech. **75**, 257 (1976).

[22] A. J. Bergou, L. Ristroph, J. Guckenheimer, I. Cohen, and Z. J. Wang, Fruit Flies Modulate Passive Wing Pitching to Generate in-Flight Turns, Phys. Rev. Lett. **104**, 148101 (2010).

[23] L. Ristroph, A. J. Bergou, G. Ristroph, K. Coumes, G. J. Berman, J. Guckenheimer, Z. J. Wang, and I. Cohen, Discovering the flight autostabilizer of fruit flies by inducing aerial stumbles, Proc. Natl. Acad. Sci. USA **107**, 4820 (2010).

[24] L. Ristroph, A. J. Bergou, J. Guckenheimer, Z. J. Wang, and I. Cohen, Paddling Mode of Forward Flight in Insects, Phys. Rev. Lett. **106**, 178103 (2011).

[25] L. Ristroph, G. Ristroph, S. Morozova, A. J. Bergou, S. Chang, J. Guckenheimer, Z. J. Wang, and I. Cohen, Active and passive stabilization of body pitch in insect flight, J. R. Soc. Interface **10**, 20130237 (2013).

[26] B. Cheng, S. N. Fry, Q. Huang, and X. Deng, Aerodynamic damping during rapid flight maneuvers in the fruit fly drosophila, J. Exp. Biol. **213**, 602 (2010).

[27] I. Faruque and J. S. Humbert, Dipteran insect flight dynamics. Part 1 Longitudinal motion about hover, J. Theor. Biol. **264**, 538 (2010).

[28] T. L. Hedrick, B. Cheng, and X. Deng, Wingbeat time and the scaling of passive rotational damping in flapping flight, Science **324**, 252 (2009).

[29] Z. E. Teoh, S. B. Fuller, P. Chirarattananon, N. O. Prez-Arancibia, J. D. Greenberg, and R. J. Wood, *Proceedings of the International Conference on Intelligent Robots and Systems* (IEEE, Piscataway, 2012), p. 3209.

[30] L. Ristroph and S. Childress, Stable hovering of a jellyfish-like flying machine, J. R. Soc. Interface **11**, 20130992 (2014).

[31] F. van Breugel, W. Regan, and H. Lipson, From insects to machines, IEEE Robot. Autom. Mag. **15**, 68 (2008).

[32] D. A. Spence, The lift coefficient of a thin, jet-flapped wing, Proc. R. Soc. London Ser. A **238**, 46 (1956).

[33] T. Schnipper, A. Andersen, and T. Bohr, Vortex wakes of a flapping foil, J. Fluid Mech. **633**, 411 (2009).

[34] D. Shiels and A. Leonard, Investigation of a drag reduction on a circular cylinder in rotary oscillation, J. Fluid Mech. **431**, 297 (2001).

[35] G. R. Spedding and A. Hedenstrom, PIV-based investigations of animal flight, Exp. Fluids **46**, 749 (2009).

[36] T. Hesselberg and F.-O. Lehmann, Turning behavior depends on frictional damping in the fruit fly Drosophila, J. Exp. Biol. **210**, 4319 (2007).

[37] W. B. Dickson, P. Polidoro, M. M. Tanner, and M. H. Dickinson, A linear systems analysis of the yaw dynamics of a dynamically scaled insect model, J. Exp. Biol. **213**, 3047 (2010).